Static crushing of aluminium tubes filled with PET foam and a GFRP skeleton. Numerical modelling and multiobjective optimization.

M. Costas[a,b,*], D. Morin[b], M. Langseth[b], J. Díaz[a], L. Romera[a]

[a]*Structural Mechanics Group, School of Civil Engineering. Universidade da Coruña. Campus de Elviña, 15071, A Coruña, Spain*
[b]*Structural Impact Laboratory (SIMLab) and Centre for Advanced Structural Analysis (CASA). Department of Structural Engineering, Norwegian University of Science and Technology (NTNU), NO-7491 Trondheim, Norway*

Abstract

This investigation focuses on the multiobjective optimization of a crash box subjected to static loading by using a validated numerical model and an analytical approach. The crash box is made with a unique combination of three materials: an aluminium tube filled with polyethylene terephthalate (PET) foam and a glass-fibre reinforced polymer (GFRP) skeleton. A finite element model was calibrated based on the results obtained in a material testing campaign using appropriate constitutive equations. A J2–plasticity model was used for the material behaviour of the aluminium alloy, and the PET foam was modelled using Deshpande and Fleck's model. Regarding the short-fibres GFRP, a Voce plasticity model was fitted to the experimental data. After a successful validation of the finite element model, the filled aluminium tube was subjected to a structural optimization to achieve the best crash performance. Three relevant design variables were selected: the thickness of the outer aluminium cylinder, the thickness of the GFRP and the density of the PET foam, the last being related to the crushing strength of the foam. Given the high computational cost of each finite element model, a multi-adaptive regression splines metamodel was fitted to a large-scale sampling. Optimum pairs were obtained for the absorbed energy, the specific energy absorption, the peak load and the mass of the component; stating the relative contribution of each design variable to the crashworthiness of the crash box and enabling the choice of a balanced optimum design. A semi-empirical model based on Hanssen's interaction formula was calibrated with the data from a validated finite element model. This analytical model was able to reproduce the behaviour of

---

*Corresponding author.
Email addresses: `miguel.costas@ntnu.no` (M. Costas), `david.morin@ntnu.no` (D. Morin), `magnus.langseth@ntnu.no` (M. Langseth), `jdiaz@udc.es` (J. Díaz), `lromera@udc.es` (L. Romera)

the component over the design region selected for the optimization, and was also used for its optimization with satisfactory results.

1. Introduction

Composites, synthetic foams and aluminium structures are gaining ground over structural steel in the automotive industry due to weight reduction and hence a decrease of pollutant emissions. However, the newer, lighter structures must also meet the criteria and standards for structural and occupant safety. More specifically, the structural parts dedicated to the absorption of the kinetic energy during an impact, in particular frontal crash boxes, must be designed so that a satisfactory level of crashworthiness is achieved with the lowest possible weight.

Foam-filled metal extrusions substantially alter the crushing behaviour of the outer thin-walled column compared to an empty tube, improving the performance of the overall structure. During axial crushing the foam acts as an elastic foundation for the metal walls, reducing the local buckling length and, therefore, enabling more progressive folds to be developed. Early works by Reid and Reddy [1, 2] investigated the axial crushing of straight and tapered mild steel tubes filled with polyurethane foam of different densities. These experimental results were used to validate the theoretical expressions for the mean crushing load later proposed by Abramowicz and Wierzbicki [3]. Numerical simulations on the axial crushing of foam-filled extrusions published in 1997 by Seitzberger et al. [4] had a good agreement with experimental results for the compression of steel tubes filled with aluminium foam. An extensive experimental campaign was carried out in the next three years (1998-2001) by Langseth et al. [5] and Hanssen et al. [6, 7] on square and circular foam-filled aluminium extrusions in different tempers and foam densities. These authors proposed an expression for the mean crushing force taking into account the strong interaction effect between the foam and the walls of the extrusions. An optimization of the filled crash boxes was published in [8]. In parallel, Santosa et al. [9] carried out an experimental and numerical study of the previous designs and validated the interaction formulas. The main conclusion from these works was that the absorbed energy can be increased with foam filler, but the increase in weight generally decreases the specific efficiency of the filled tube compared to an empty extrusion, expressed in relative terms. Recent work on foam-filled sections trends to incorporate natural materials [10].

The numerical optimization of foam-filled extrusions has been an active research topic during the past decade. Zarei and Kröger [11] optimized the crashworthiness of square hollow sections filled with aluminium foam or honeycomb using finite element simulations and surrogate models. A similar work was published in 2009 by Hou et al. [12]. Multi-tubular foam-filled structures were optimized by Bi et al. [13] and a series of research articles were published from 2010 on the optimization of sections filled with graded foams [14], foam-filled conical tubes [15], bi-tubal structures [16], tapered square tubes [17] and single and bi-tubal polygonal geometries [18]. A recent state-of-the-art review of crashworthiness optimization can be found in [19].

Considerable research effort has also been focused on the use of fibre-reinforced plastics in combination with metals for crashworthiness applications due to their superior specific energy absorption. Fibre-resin composites have high strength-to-weight ratios compared to metals, but their crushing is typically dominated by brittle, unstable failure modes. A relatively recent advent in crashworthiness engineering is the design of externally-wrapped, fibre-reinforced metal tubes. This innovation means that the ductile metal crushing modes are combined with the high strength and brittle fracture of the fibres, with no impairment of the predictability or stability of the overall system [20]. The first theoretical study on the progressive axial crushing of externally reinforced fibre-metal tubes was published by Hanefi and Wierzbicki [21] in 1996, where the authors proposed a theoretical model based on Alexander's idealization for metal tubes [22]. Further experimental studies were conducted by Song et al. [23] and Shin et al. [24] in 2000 and 2002, respectively. More recent works by Bambach and Elchalakani studied the theoretical [25] and experimental crushing [26, 27] of CFRP-wrapped steel tubes. The general conclusion is that the mean crushing load and the specific energy absorption can be increased with this kind of external reinforcement compared to the sum of the contributions from each material without considering any interaction effect.

The inner reinforcement of metal tubes with composite structures has been recently studied by Costas et al. [28, 29], motivating the present investigation. The beneficial contribution of an inner GFRP skeleton to the crashworthiness of a steel tube was stated, but it was also observed that the efficiency of the design could be significantly enhanced with some kind of constraining or confinement system which prevented the GFRP parts from falling apart after incipient fracture. Thus, an additional PET foam filler was added to a GFRP-reinforced aluminium tube in order to improve the performance of the component (Figure 1). The experimental campaign carried out [30] produced promising results as a

3

remarkable interaction between both filler materials (GFRP and PET foam) was found. This was also quantified by means of a modification of Hanssen's formula [6, 7].
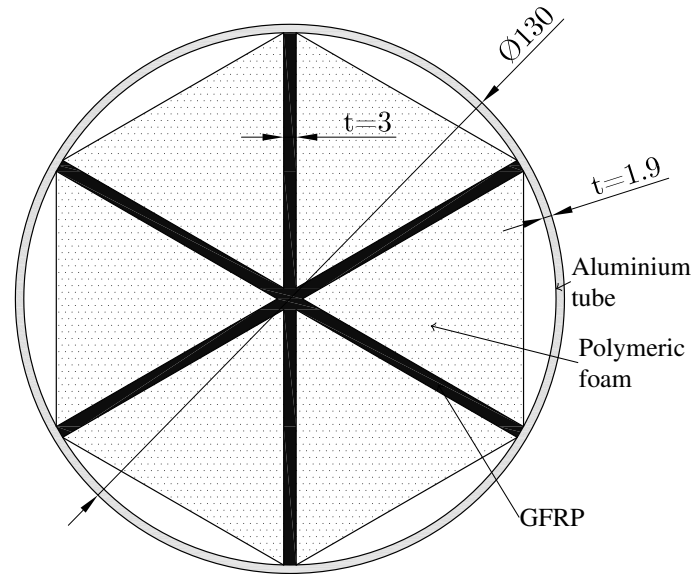

Figure 1: Cross-section of the proposed crash box, experimentally investigated in [30]. Dimensions in millimetres.

The new contribution in the present work is the structural optimization of quasi-static behaviour of the crash box shown in Figure 1, with a unique combination of three materials. The optimization was carried out using numerical simulations and an analytical approach developed to reproduce the behaviour of the component. Thus, a finite element model was built using material testing data to fit the appropriate constitutive models. A novel treatment was given to the short-fibres GFRP; an elastic-plastic model was considered as a constitutive equation for simplicity, which provided the desired behaviour. The response of the finite element model at a set of points in the selected design region was then recorded, and an adequate metamodel was fitted to the results. The analytical approach was developed by means of Hanssen's modified equation recently proposed in [30], which was also fit to the sample data from the simulations with a good degree of accuracy. A genetic multiobjective optimization algorithm was run on the metamodel and the analytical model, and different Pareto sets were obtained for selected objective functions matching the crashworthiness criteria. These optimum sets contain the best-performing designs and provide a valuable tool to understand the influence of the design variables on the performance of the component.

2. Finite element simulations

2.1. Material models and identification of parameters

This section presents the fit of selected material constitutive models to the obtained experimental results. Each model takes into account the most relevant characteristics of each material.

2.1.1. AA6063-T5 aluminium alloy

A von Mises yield condition with isotropic hardening was employed:

$$f(\boldsymbol{\sigma}, p) = \sigma_{\mathrm{eq}}(\boldsymbol{\sigma}) - (\sigma_0 + R(p)), \tag{1}$$

where σ_{eq} is the von Mises equivalent stress, p is the equivalent plastic strain defined in terms of the incremental plastic strains $\mathrm{d}\varepsilon_{ij}^{\mathrm{p}}$ as $p = \int \sqrt{\frac{2}{3}\mathrm{d}\varepsilon_{ij}^{\mathrm{p}}\mathrm{d}\varepsilon_{ij}^{\mathrm{p}}}$, σ_0 is the initial yield strength and the term $R(p)$ controls the isotropic hardening, which consisted of a two-term Voce law [31]:

$$R(p) = \sum_{j=1}^{2} Q_j \left[(1 - \exp\left(-b_j p\right)\right]. \tag{2}$$

In this equation, Q_j and b_j are material parameters to be calibrated through tensile tests in the extrusion direction. As no failure was observed in the extrusions during component testing, this was not accounted for in the numerical model.

The values for the model parameters obtained from the tensile tests described in [30], with a least-squares fit up to diffuse necking, are provided in Table 1.

Table 1: Material properties and model parameters of aluminium alloy AA6063-T5 in circular extrusion.

Property or parameter	Value
Density, ρ [t/m^3]	2.56
Young's modulus, E [GPa]	53.84
Poisson ratio, ν	0.33
σ_0 [MPa]	204.94
Q_1 [MPa]	60.28
b_1	19.24
Q_2 [MPa]	3.95
b_2	3078.86

True stress-strain curves from tensile experiments [30] and simulations are provided in Figure 2, and show an excellent correlation between numerical and experimental data

up to diffuse necking. For larger strains beyond this point, the model extrapolated the stress values according to the Voce parameters previously fitted.
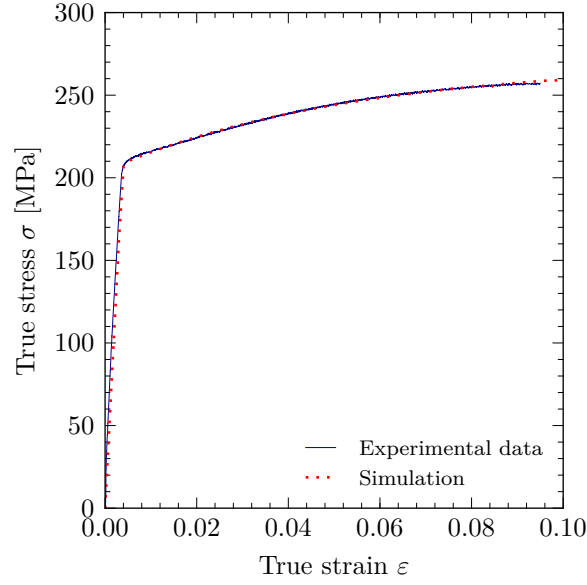

Figure 2: AA6063-T5 true stress-strain curves obtained from experimental tensile tests [30] and numerical simulation.

2.1.2. Glass-fibre reinforced polyamide

The Ultramid A3WG10 BK00564 GFRP was modelled isotropically with a failure criterion governed by the equivalent plastic strain. The von Mises yield criterion was used, and the hardening was described with a Voce law with two terms to fit the experimental curve, shown in Figure 3. Thus, the equation governing hardening reads:

$$\sigma_{\mathrm{y}} = \sigma_0 + \sum_{j=1}^{2} Q_j \left[1 - \exp\left(-b_j p\right)\right], \tag{3}$$

where σ_0 is the initial yield stress, set to 25 MPa, p is the equivalent plastic strain, and Q_j, b_j are the parameters to be calibrated.

Fracture of GFRP was modelled through a criterion based on the value of the equivalent plastic strain [32, 33]. The finite element code activates the damage in an element if its accumulated equivalent plastic strain reaches p_{u} at all section points at any one integration point, i.e.,

$$\int \frac{\mathrm{d}p}{p_{\mathrm{u}}} = 1, \tag{4}$$

removing the element from the mesh. The value of the integral, which is discretized for each increment in the finite element code, increases monotonically with each increment of the plastic strain. The reader is referred to [32, 33, 34] for details. From the experimental

6

Table 2: Material properties and model parameters of the GFRP Ultramid A3WG10 BK00564.

Property or parameter	Value
Density, ρ [t/m^3]	1.55 [35]
Mean Young's modulus, E [GPa]	15.52
Poisson ratio, ν	0.4 [35]
σ_0 [MPa]	25.00
Q_1 [MPa]	132.03
b_1	272.49
Q_2 [MPa]	52.01
b_2	4758.28

campaign in [30], a value of $p_u = 0.0107$ was adopted for the ultimate equivalent plastic strain, which corresponds to a total strain of 0.0238 (sum of the elastic an plastic strains).

Table 2 summarizes the material properties and the model parameters of the glass-fibre reinforced polymer Ultramid A3WG10 BK00564. Stress-strain curves obtained from the tests and simulations are compared in Figure 3.
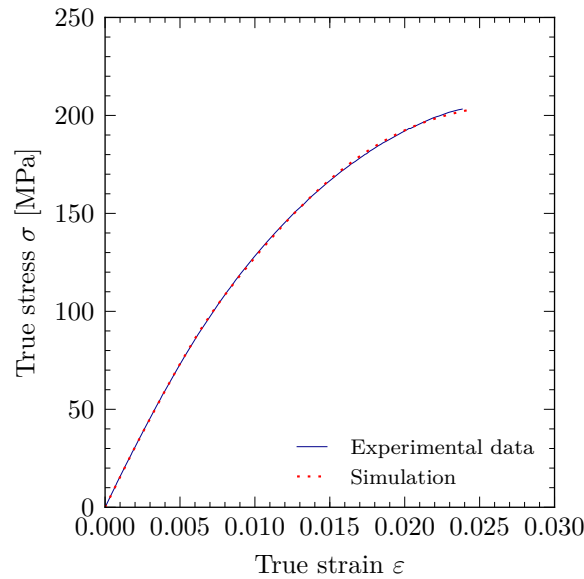

Figure 3: True stress-strain curves obtained from experimental uniaxial tests and numerical simulations of Ultramid A3WG10 BK00564.

2.1.3. PET-based polymeric foam

The polymeric foam ArmaFORM PET/W AC 135 is an orthotropic material due to its manufacturing process involving extrusion. If this foam is crushed along its manufactured direction a higher crushing strength is observed. In [30], the foam was placed inside the aluminium extrusion so that it was crushed in a direction orthogonal to the manufactured

direction, resulting in a lower crushing strength. In the current investigation, both directions were considered separately for the optimization of the component. The foam was modelled isotropically using the following two approaches; 1) using the properties in the weak direction, and 2) with the properties in the strong direction. The stress-strain curves and relevant mechanical properties were thus obtained for specimens taken parallel and normal to the manufactured direction of the foam. The foam was modelled through an elastic-plastic model with isotropic hardening originally developed for metallic foams by Deshpande and Fleck [36] and included in Abaqus as *crushable foam*. The yield surface f includes pressure dependency in addition to deviatoric stresses. In particular, the expression for f is an origin-centred ellipse in the σ_H–σ_{eq} plane which evolves proportionally in hardening governed by the equivalent plastic strain p. The expression for this yield surface f reads

$$f = \sqrt{\sigma_{eq}^2 + \alpha^2 \sigma_H^2} - B = 0, \tag{5}$$

where σ_{eq} is the von Mises equivalent stress and $\sigma_H = I_\sigma/3$ is the hydrostatic stress. The factor α defines the shape of the ellipse according to the ratio of the initial yield strength in uniaxial compression to the initial yield strength in hydrostatic compression (see [36, 34]). The latter was obtained experimentally in a triaxial compressive test (see Figure 4), leading to a value of $\alpha = 0.729$. This ratio of yield strengths was assumed to be the same in both working directions. Given that the gaps between the foam and the extrusion walls in the component were not closed, the lateral confinement levels of the foam parts were not expected to be high enough to imply relevant differences derived from this assumption. It is worth remarking that in [30], the major contribution to the interaction between different materials to the crushing strength of the component was observed between the foam and the GFRP (more fracture was observed in the GFRP due to the interaction with the foam), whereas a negligible interaction was reported between the foam and the aluminium tube due to these gaps.

In Equation (5), B is the current size of the vertical (σ_{eq}) axis of the yield ellipse, defined in [36, 34] as a function of the current compressive yield stress and α.
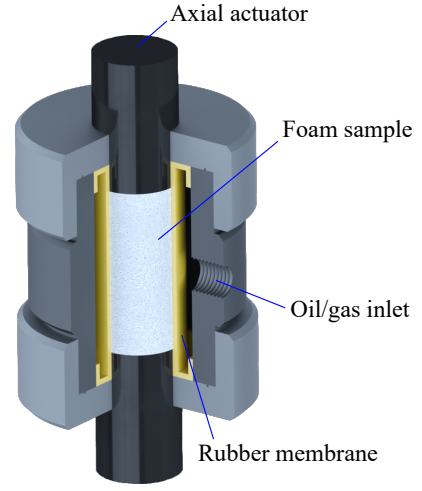
A flow potential g was adopted, reading

$$g = \sqrt{\sigma_{eq}^2 + \beta^2 \sigma_H^2} = 0, \tag{6}$$

so that the model was flexible enough to represent non-associated flow. This equation is
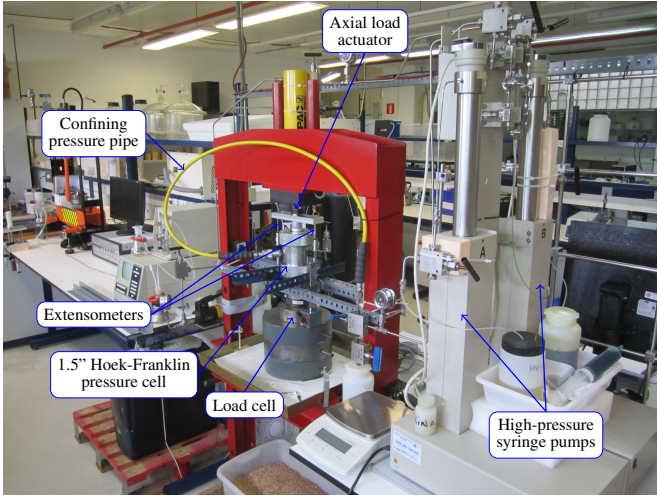
(a) Test set-up.

(b) Schematic illustration of the Hoek-Franklin pressure cell.

Figure 4: Triaxial compression machine for the experimental determination of the parameter α of Deshpande and Fleck's model, depending on the ratio of the uniaxial yield stress to the hydrostatic yield stress.

in the same form as f, but with a different shape parameter, meaning that if $\beta = \alpha$ then $\frac{\partial g}{\partial \sigma} = \frac{\partial f}{\partial \sigma}$, and the flow is associated. According to [36, 34], the factor β can be expressed in terms of the plastic Poisson's ratio v^{p} as follows:

$$\beta = \frac{3}{\sqrt{2}} \sqrt{\frac{1 - 2v^{\mathrm{p}}}{1 + v^{\mathrm{p}}}}. \tag{7}$$

This allowed β to be obtained from a simple uniaxial compression test in which the transverse plastic strains were measured.

Meeting the requirements of ISO 844:2014 [37], foam specimens were extracted and subjected to uniaxial compression along the directions parallel and orthogonal to the extrusion direction in the foam production line. An assumption was made when it came to obtaining the plastic Poisson's ratio v^{p}, customarily defined for isotropic materials as the ratio of the transverse plastic strains to the plastic strain in the load direction. The mean value of both transverse directions was used to obtain the transverse plastic strain. According to this, the values of v^{p} and β for both directions are the ones provided in Table 3. The value of β is different from α, so the material exhibits non-associated plastic flow.

The hardening curve has been included in the finite element model through a direct input of the yield stress–uniaxial plastic strain pairs obtained from the uniaxial compression tests.

Table 3 contains a summary of the mechanical properties of the PET foam in the weak and strong directions. The experimental and numerical stress-strain curves for quasi-static

Table 3: Material properties and model parameters of ArmaFORM PET/W AC 135 PET-based foam for different loading directions. An asterisk indicates that the value was obtained assuming the same α coefficient obtained for the weak direction of the foam.

Property or parameter	Orthogonal to extrusion	Parallel to extrusion
Density, ρ [t/m^3]	0.135	0.135
Young's modulus, E [MPa]	20.41	59.01
Elastic Poisson ratio, ν	0.1	0.1
$\sigma_{0.3}^{\mathrm{C}}$ [kPa]	982.98	2529.97
$\sigma_{0.3}^{\mathrm{H}}$ [kPa]	1383.30	*3465.71
α	0.73	*0.73
Plastic Poisson's ratio ν^{p}	0.09	0.07
β	1.84	1.72

loading are plotted in Figure 5. In Table 3, $\sigma_{0.3}^{\mathrm{C}}$ and $\sigma_{0.3}^{\mathrm{H}}$ represent the plateau stresses – obtained for a true strain of 0.3– under uniaxial and hydrostatic compression, respectively.
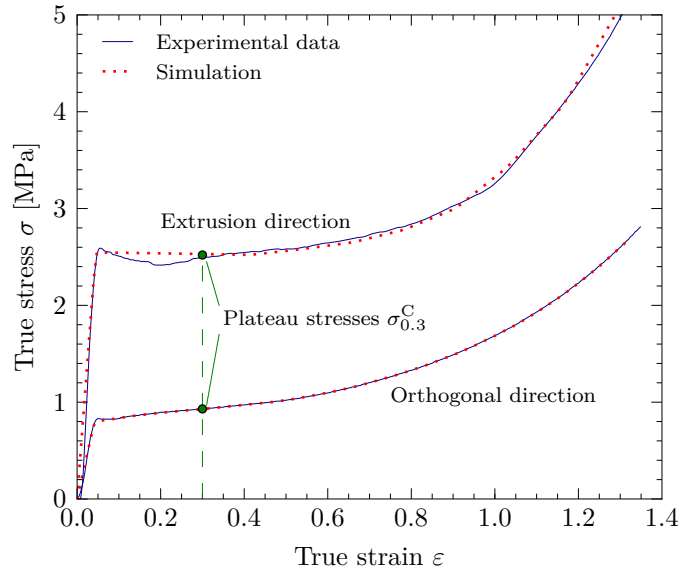

Figure 5: True stress-strain compressive curves from uniaxial tests and simulations for Armaform PET/W AC 135 PET-based foam in different directions.

2.2. Component model

A detailed finite element model of the crash box subjected to quasi-static loading has been constructed using the Abaqus Explicit package. This model was validated against the quasi-static experimental results obtained in [30].

The metal tube, with a thickness of 1.9 mm in the baseline design, was modelled using a fine mesh of 1.5×1.5 mm, four-node linear shell elements with five integration points

through the thickness and with reduced integration, which allowed the tube to develop the correct folding pattern while keeping a good thickness-to-length ratio. The contact algorithm accounted for the element thickness to avoid any undesired shifting of the force-displacement curves due to self-contact during folding. The end of the tube in contact with the loading plate was triggered according to the ring pattern applied to the experimental specimens [30] to ensure that the same collapse mode was initiated, Figure 6b. These triggers were formed at a previous step by imposing a radial displacement of 1.2 mm directed inwards at the edge of the tube.

GFRP sheets, with a thickness of 3 mm in the baseline design, were modelled using the same four-node linear shell elements with an element size of 3 mm. Given that a fracture algorithm based on element deletion was adopted, the element size had to be small enough to represent fracture in the GFRP parts. The GFRP structure was modelled respecting the mechanization process in which three independent sheets were assembled together without any adhesive, in the way shown in [30]. It is also worth mentioning that in the same way as it was done in [30] the height of the GFRP parts is 2 mm lower than the height of the aluminium tube and the foam. This was done to avoid an overlap of the initial peak forces.

Finally, the foam prisms were modelled with eight-node, linear solid elements with an average size of 5 mm. The critical aspect governing the element size of these parts is the fact that the foam should be able to be captured inside the folds during crushing. This was also a challenge for the convergence of the analysis, since some elements captured in the folds experienced extreme distortions which decreased the stable time increment and influenced the overall convergence. To avoid or minimize this problem, a distortion control for the foam parts was included, which locked those elements undergoing volumetric deformation greater than 95 %. It was observed that only a few elements had to be locked in order to guarantee the convergence of the simulations.

Two additional parts were included in the model: a support reaction plate and a moving loading plate, which crushed the component. These were modelled through rigid elements and a rigid body constraint. A friction coefficient of 0.2 was assumed in the contact between the plates and the component. In order to speed up the simulations and reduce the required number of time increments, a time scaling factor of 1200 was applied to the loading rate, meaning that the quasi-static experimental crushing at 50 mm/min was simulated at 10 m/s. In order to avoid undesired inertial effects, the speed of the moving plate was smoothly ramped up from 0 to 10 m/s. Additionally, the kinetic energy

(a) Finite element model of the crash box. The different parts have been partially disassembled for a better view.

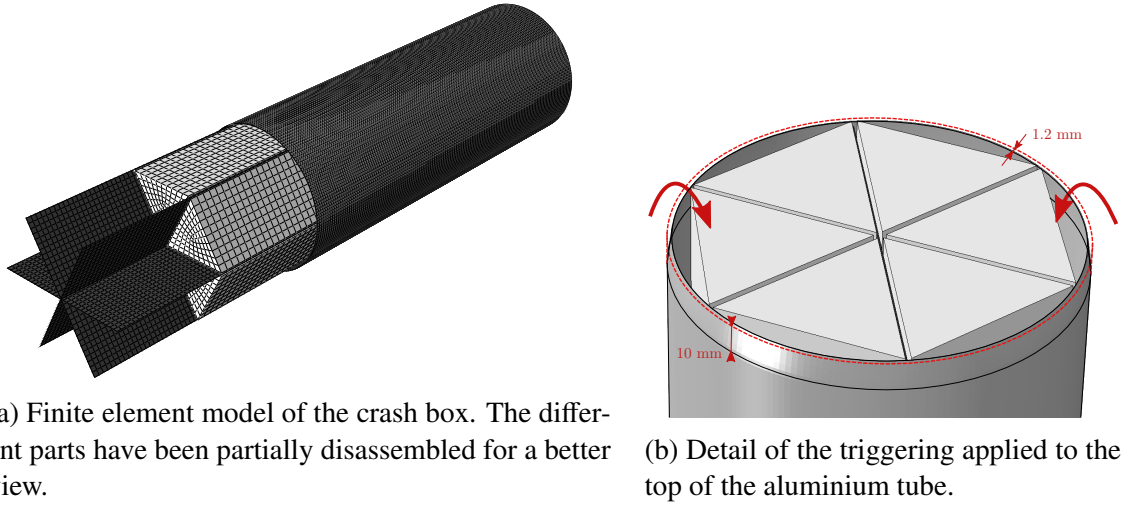(b) Detail of the triggering applied to the top of the aluminium tube.

Figure 6: Finite element model: geometry, mesh, and detail of the triggering scheme.

was checked during the simulation so that it did not exceed a small percentage of the total energy at any time. The maximum percentage was 2% in the current simulations. This technique was used in other investigations for the simulation of quasi-static crushing [38]. The component was crushed to a total length of $245\,\text{mm}$, which equated a 70% of its total length. Analyses were run in parallel with two cores dedicated to each simulation. Despite being considerably slower, loop parallelization was preferred to a faster domain-based strategy, due to the fact that the latter can produce differences in the results depending on the number of domains.

A view of the finite element model is shown in Figure 6a. Loading and support plates are removed for a better view, and the different parts are partially disassembled.

2.3. Validation of the finite element model of the component

The finite element model was validated against the quasi-static crushing tests performed at $50\,\text{mm/min}$ [30]. Figures 7a and 7c show that good agreement was obtained, with the exception of the initial peak. In Figure 7c, the average force of the simulation is provided as a function of the axial crushing length, which is the integral of the force-displacement curve divided by the current displacement δ, as follows:

$$F_{\text{avg}}(\delta) = \frac{\int_0^\delta F(\delta)\,\text{d}\delta}{\delta}. \tag{8}$$

The average force is lower than that of the experimental tests in the first part of the crushing, but it eventually reaches the experimental curves at the end of the crushing. The average force at the end of the crushing was used to obtain the values of energy absorp-

tion shown in Figure 7a.

The GFRP sheets used for the experimental components in [30] presented imperfections due to the use of a single inlet for the injection of the parts, and also due to the high fibre content. These imperfections had a wavelike form and caused also some misalignment with respect to the longitudinal axis of the component when assembled. To account for these combined geometrical imperfections in the numerical model, these defects were represented in the numerical model as shown in Figure 8. As no direct measurements were carried out to reveal the magnitude of these imperfections, a sensitivity analysis was performed by varying the amplitude in Figure 8. To that end, simulations were run with initial imperfections of 1.0, 2.0 and 3.0 mm applied to the top part of the GFRP sheets according to the pattern depicted in Figure 8, resulting in the initial peak loads provided in Table 4 and the force-displacement curves presented in Figure 7b. When imperfections were applied, the remaining part of the curve was even more similar to the experimental behaviour of the component. This could indicate that the imperfections in the GFRP sheets actually enable a more progressive degradation of the composite. This has been checked in the simulations and it has been found that the imposed imperfections in the GFRP triggered a stronger interaction with the foam, leading to a more intensive degradation of the GFRP and a higher crushing force. The effects derived from a misalignment of the GFRP were also observed in [28].

The analytical value of the mean crushing force obtained by the fit of Hanssen's modified equation provided in Section 3.2 is also given in Figure 7c. This is in agreement with the experimental and numerical data. The value of the analytical mean crushing force was obtained for the total crushing length.

Table 4: Effect of an initial misalignment of the GFRP parts (FE) on the initial peak during the axial crushing of the component, according to Figure 8.

| Initial misalignment [mm]	Initial peak force P_{peak} [kN]
0.0 (straight edges)	158.67
1.0	144.06
2.0	132.80
3.0	126.51

In Figure 9, the predicted crushing process is shown and compared with the images from the quasi-static experimental tests. Overall, the agreement between the finite element model and the experimental tests was very good, thus the model was considered to be
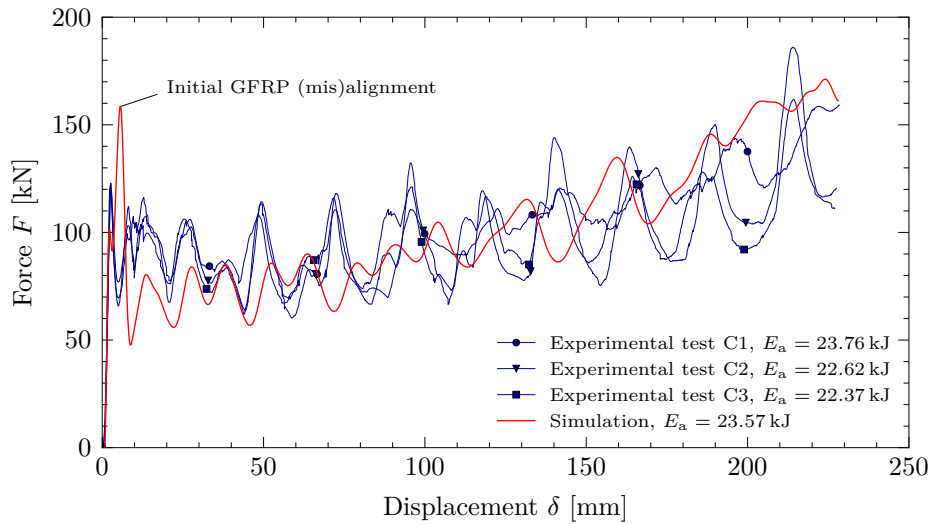
(a) Force-displacement curves and absorbed energy of the quasi-static axial crushing of the experimental components C1, C2 and C3 (see [30]), and the finite element model.
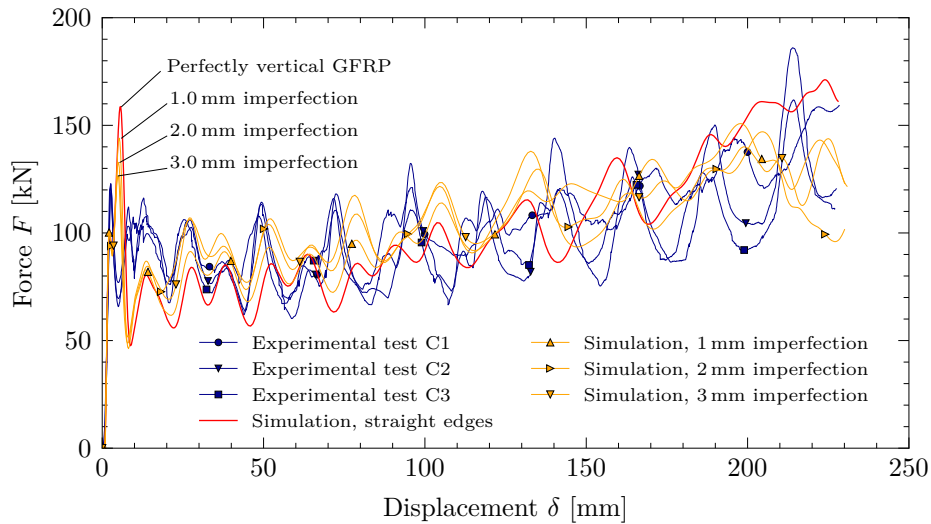
(b) Comparison of the force-displacement curves obtained from experiments and FE simulations with imperfections of different magnitudes.
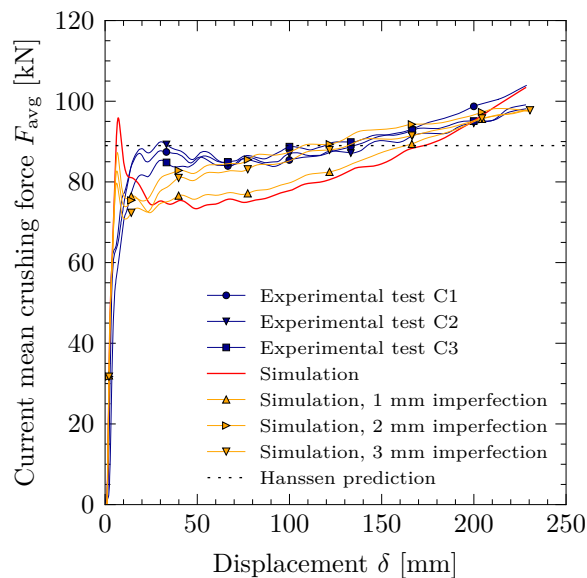
(c) Average crushing force-displacement curves of the experimental components C1, C2 and C3 (see [30]), and the finite element model with different imperfections in the GFRP parts, together with Hanssen's analytical prediction, Equation (15).

Figure 7: Crushing force-displacement curves of experimental components C1, C2 and C3, and the finite element model, with and without imperfections.
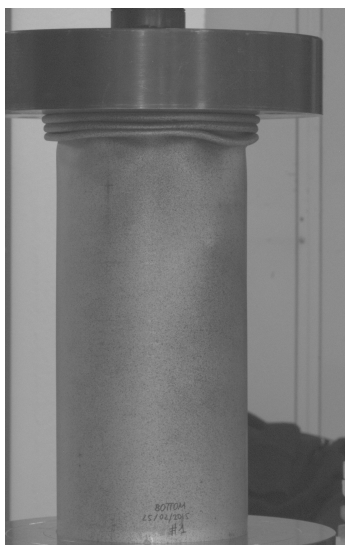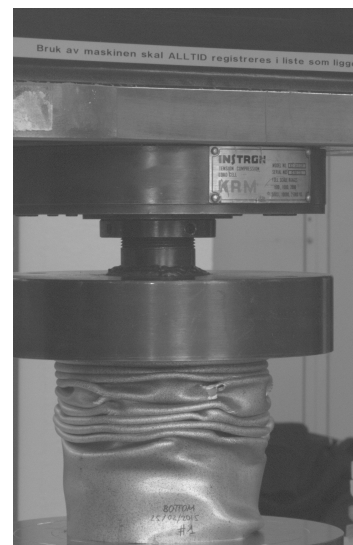
14
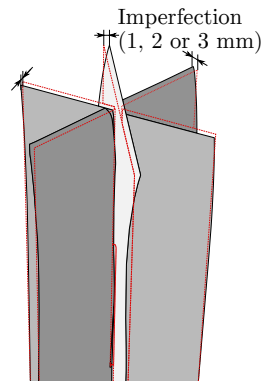
Figure 8: Scheme of the imperfections applied to the top of the GFRP sheets (scaled). Red dotted lines represent the undeformed geometry. (For interpretation of the references to color in this figure legend, the reader is referred to the web version of this article).
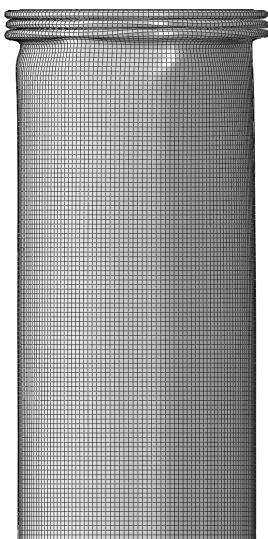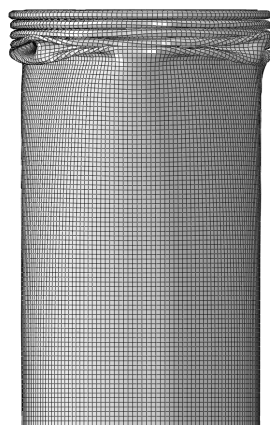

(a) Quasi-static test, δ = 67.5 mm.

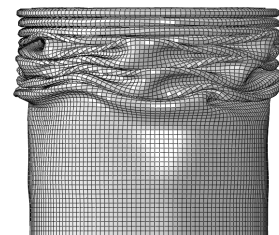(b) Quasi-static test, δ = 126.77 mm.

(c) Quasi-static test, δ = 228.33 mm.

(d) Simulation, δ = 67.5 mm.

(e) Simulation, δ = 126.77 mm.

(f) Simulation, δ = 228.33 mm.

Figure 9: Image sequence of the experimental test and the finite element simulation. The same crushing mechanism was observed.

accurate and reliable enough to be used for the optimization of the component. Moreover, given that the behaviour of the component was almost similar when subjected to quasi-static and impact loading conditions [30], the current finite element model could be safely employed for impact simulations up to 10 m/s.

3. Multiobjective optimization

3.1. Problem statement and methodology

Five metrics were initially considered as candidates to become the objective functions for the optimization problem:

- The component mass m.

- The absorbed energy E_a, defined as the integral of the measured force $F(\delta)$ over the crushed distance δ, i.e.,

$$E_a = \int_0^{\delta_{max}} F(\delta)\, d\delta. \tag{9}$$

- The specific energy absorption *SEA*, defined as the ratio of the absorbed energy E_a to the mass of the component m,

$$SEA = \frac{E_a}{m}. \tag{10}$$

- The initial peak load P_{peak}.

- The crush force efficiency *CFE*, defined as the ratio of the mean crushing force P_m to the initial peak load P_{peak},

$$CFE = \frac{P_m}{P_{peak}}. \tag{11}$$

All of these are quantities that should be either minimized (m, P_{peak}) or maximized (E_a, *SEA*, *CFE*) in a design optimization procedure. Given that some of these metrics oppose each other (e.g. absorbed energy vs. mass), an unconstrained, multi-objective optimization was set out for pairs E_a vs. m and *SEA* vs. P_{peak} for different material configurations. The crush force efficiency was discarded from the optimization given the relative inaccuracy of the surrogate model, which was unable to precisely reproduce the behaviour of this function (see values of the likelihood estimators in Tables 7 and 8). It is convenient to indicate here that the algorithm searched the maximum force in the initial

16

15 % of the filtered force-displacement curves to account for among other factors possible secondary peak force produced by the GFRP plates.

Regarding the design variables, it was considered that the thicknesses of the tube and the GFRP sheets, together with the foam density (proportional to its yield stress), were the most interesting aspects of the current design. The diameter of the aluminium tube, measured from the middle of the walls, was kept constant. The width of the GFRP sheets was modified accordingly so that they fitted into the tube in all cases. Regarding the foam density, even though the supplier provides six different possible densities for the PET foam [39], each with a different yield stress, this variable was considered to be continuous. The relationship between the foam density and its yield stress in the extrusion direction could be established by a simple linear fit of the products in the brochure (see Figure 10). This gave the following expression for the initial yield stress σ_0^y:

$$\sigma_0^y \, [\text{MPa}] = 0.0021899\rho \left[\text{kg/m}^3 \right] - 0.7219274. \tag{12}$$

Here, it was assumed that the yield stresses of the foam loaded in its weak direction follow the same linear relationship, scaled by the ratio of the plateau stresses $\sigma_{0.3}^C$ of the strong and weak directions, i.e. 2.57.
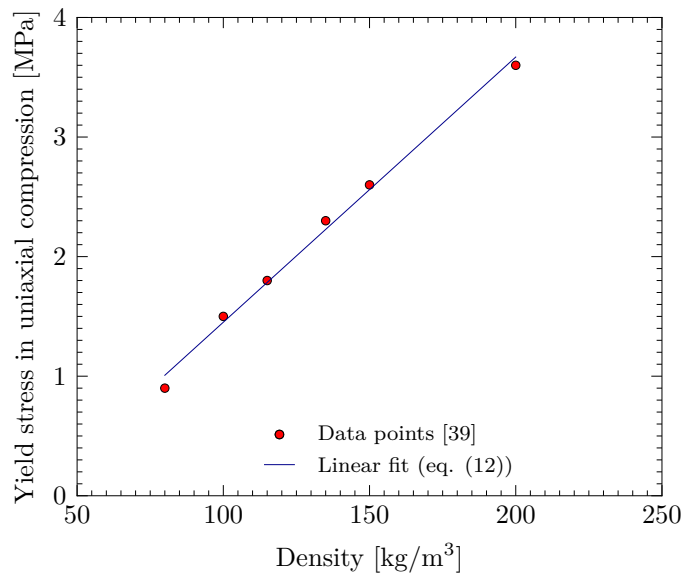

Figure 10: Linear fit to the density-yield stress pairs provided for Armaform PET/W AC PET-based foams, load direction parallel to extrusion direction. $R^2 = 0.99416$.

Two different optimization cases were studied:

- Case I consisted of the optimization of the same component experimentally studied in [30], i.e. the foam was placed so that it was crushed along its weak direction.

17

- Case II consisted of the same optimization as in Case I, but with the foam loaded in its strong direction.

The ranges of the design variables are presented in Table 5.

Table 5: Ranges of the design variables for the optimization algorithm.

Design variable	Lower bound	Upper bound
Tube thickness [mm]	1.00	4.00
GFRP thickness [mm]	1.00	5.00
Foam density [kg/m^3]	80.00	200.00

The optimization algorithm was run on metamodels of the objective functions given the high computational cost of each evaluation of the function. In order to build these metamodels, the design space was seeded with 400 sample points following a Latin hypercube sampling distribution (LHS). The sample size is relatively large for this kind of study, but as long as all the simulations were computed in parallel in a high-performance cluster, the computational cost of the sampling was acceptable. The use of a relatively large number of sample points can also be beneficial for obtaining a reliable Pareto front because the boundaries of the feasible region should be accurately defined.

The objective functions were obtained from the sample points and the resulting set was utilized to build a surrogate model for each response function. The computation time for each simulation was between 20–50 minutes. Given the good results found in [29, 40], a multivariate adaptive regression splines (MARS) model [41, 42] was fitted to the sampling results with acceptable likelihood estimators, provided in Section 4 for each optimization case. A description of this metamodel is provided in [43].

The genetic multi-objective optimization proposed by Eddy and Lewis [44] was used, with a population size of 300 individuals, a mutation rate of 0.1, a crossover rate of 0.8, 50 elitist individuals and a maximum number of function evaluations equal to 500 000. With this configuration, the execution time of the optimization algorithm was about 30 minutes.

3.2. Fitting of Hanssen's modified equation to the FE sample points

Hanssen et al. [6, 7] proposed an equation to predict the average crushing force of foam-filled aluminium tubes, reading

$$F_{\text{avg}} = F_{\text{avg}}^0 + A_{\text{f}}\sigma_{\text{f}} + C_{\text{avg}}\sigma_{\text{f}}^{\alpha}\sigma_0^{(1-\alpha)}b_{\text{m}}^{\beta}h^{(2-\beta)}, \tag{13}$$

18

where F_{avg} is the total average crushing force, F_{avg}^0 is the average crushing force of the empty aluminium tube, σ_{f} is the yield stress of the aluminium foam, A_{f} is the cross-sectional area of the foam, σ_0 is the yield stress of the aluminium alloy, $b_{\mathrm{m}} = b - h$, and b and h are the outer diameter and wall thickness of the aluminium tube, respectively. Lastly, C_{avg}, α and β are parameters to be calibrated.

In [30], a modification of the original formula was proposed in order to account for an inner GFRP reinforcement interacting with the foam. Unlike the aluminium tube and the foam, the contribution of this GFRP reinforcement is exclusively linked to the interaction part of the formula because the GFRP skeleton would buckle and fracture if crushed alone. Therefore, its contribution was included adding the ultimate tensile stress of the GFRP in the interaction parameter of Equation (13), i.e.

$$F_{\mathrm{avg}} = F_{\mathrm{avg}}^0 + \sigma_{\mathrm{f}} A_{\mathrm{f}} + C_{\mathrm{avg}} \sqrt[3]{\sigma_{\mathrm{f}} \sigma_0 \sigma_{\mathrm{u}}} b_{\mathrm{m}} h. \tag{14}$$

In the current investigation, this last formula in its general form was fitted to the results from the simulations in the FE sampling and used for the optimization of the component, in addition to the MARS metamodel. To account for the effects of different thicknesses of the GFRP parts on the crushing force, the term g, representing the GFRP thickness, was added to the interaction term of the formula together with its corresponding exponent as a parameter to calibrate. Therefore, Equation (14) was generalized into

$$F_{\mathrm{avg}} = F_{\mathrm{avg}}^0 + \sigma_{\mathrm{f}} A_{\mathrm{f}} + C_{\mathrm{avg}} \sigma_{\mathrm{f}}^{\alpha} \sigma_0^{\beta} \sigma_{\mathrm{u}}^{\gamma} b_{\mathrm{m}}^{\delta} h^{\eta} g^{\lambda} \tag{15}$$

and fitted to the 400 simulation results of each sampling, i.e., for the strong and the weak directions of the PET foam equally.

To guarantee the dimensional consistency of Equation (15), the conditions $\alpha + \beta + \gamma = 1$ and $\delta + \eta + \lambda = 1$ had to be enforced. All parameters except C_{avg} were allowed to take negative values, as long as the dimensional consistency was ensured. The fit of the parameters was performed so that the root mean squared error (RMSE) between the FE-sampled values and Equation (15) was minimized. The likelihood estimators are presented in Table 6 for the two directions of the foam.

In the light of these results, a better fit was obtained when the foam was placed in its weak direction, i.e., for lower yield strengths. In any case, the fit was considered accurate enough to be used for the optimization of the component. The results arising

Table 6: Best-fitting parameters for Hanssen's modified equation considering the foam filler working in its two directions. The generalized equation was fitted to the simulations, with a crushing length of 245 mm (70 % of the total length). RMSE: root-mean-squared error, MAE: maximum absolute error.

Foam direction	α	β	γ	δ	η	λ	C_{avg}	RMSE [kN]	MAE [kN]
Weak	2.27	-1.14	-0.13	0.78	-0.24	0.46	2.76	3.02	12.26
Strong	2.56	-1.73	0.17	0.70	-0.13	0.42	1.69	6.26	22.62

from the optimization of the analytical formula are compared to the MARS prediction in Section 5.

## 4. Results of the multiobjective optimization

4.1. Case I: Foam loaded in its weak direction

The likelihood of the surrogate model was checked by means of the goodness indicators provided in Table 7. Good agreement was achieved for all the proposed functions except the crush force efficiency.

Table 7: Goodness estimators of the MARS surrogate model fitted to the sample points in optimization case I. RMSE: root-mean-squared error, MeanAE: mean absolute error.

Objective function	R^2	RMSE	MeanAE
Absorbed energy	0.9984	0.4309 kJ	0.310 kJ
Mass	0.9999	3.349×10^{-4} kg	2.432×10^{-4} kg
Specific energy absorption	0.9964	0.200 kJ/kg	0.150 kJ/kg
Initial peak load	0.9990	1.871 kN	1.445 kN
Crush force efficiency	0.8066	0.537	0.278

Pareto fronts considering E_a vs. m and SEA vs. P_{peak} are provided in Figure 11 and Figure 12, respectively. The values of the objective functions in the design studied experimentally in [30] are marked with a green star for easy comparison. It is important to warn the reader about the merely illustrative value of this mark: given the alignment defects observed in the GFRP structure of the experimental components, the numerical value of the peak load was preferred to the experimental measurement to be considered here as the reference value, for a more consistent comparison with the remaining –numerical– results where the peak load is higher (see Figure 7a). In order to analyse the evolution of the design variables along the Pareto front, projections on the horizontal axes were done, and the values of the variables were plotted on these new graphs (Figures 11 and 12).
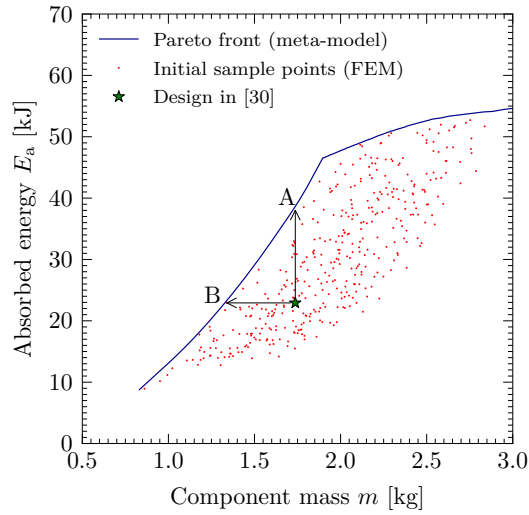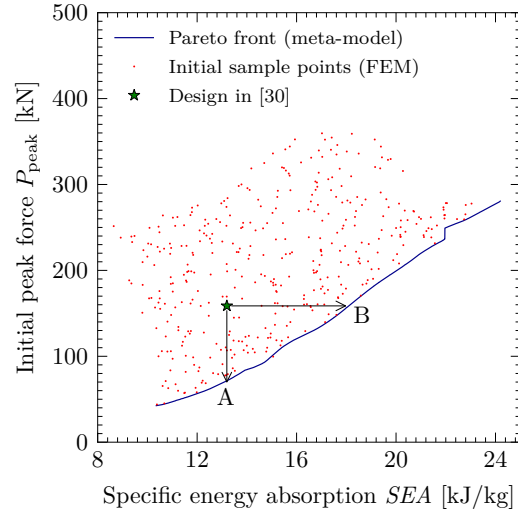
(a) Pareto front for optimization case I considering the absorbed energy and the mass of the component as objective functions.
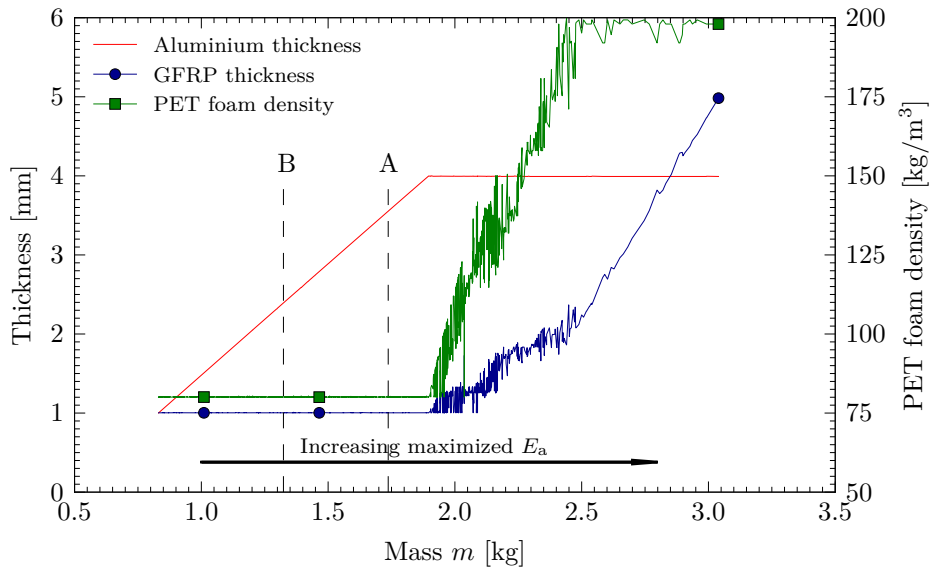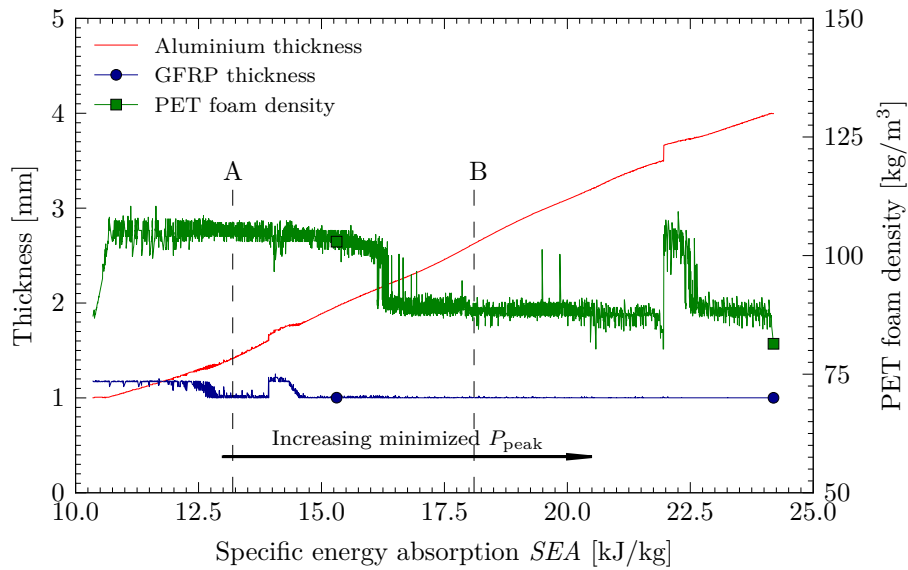

(b) Evolution of the three design variables along the Pareto front. Projection on the mass function.

Figure 11: Optimization results for case I considering the absorbed energy E_a and the component mass m as objective functions. Pareto set and evolution of the design variables.

(a) Pareto front for optimization case I considering the initial peak load and the specific energy absorption as objective functions.

(b) Evolution of the three design variables along the Pareto front. Projection on the specific energy absorption function.

Figure 12: Optimization results for case I considering the specific energy absorption *SEA* and the peak load P_{peak} as objective functions. Pareto set and evolution of the design variables.

The obtained results revealed some remarkable facts. First, the aluminium tube plays the main role in this design. This can be drawn from Figure 11b, where it can be seen that increasing the aluminium thickness is the best way to achieve the optimum performance of the component. It was only after this variable reached its upper bound that the remaining variables started to increase. The relative merits of the aluminium tube can also be observed in Figure 11a, which shows that the slope of the Pareto front increases rapidly as the aluminium thickness grows, and then increases at a lower rate when this thickness reaches its upper bound and the other materials come into play. A second remarkable fact is that the performance of the design studied in [30], marked with the green star, can easily be improved in one way or another:

- Its absorbed energy can be improved by approximately 52 % if the aluminium thickness is increased to 3.55 mm, the foam density is set to 80 kg/m^3 and the GFRP thickness is reduced to 1.0 mm (lower bounds). This is graphically indicated in Figure 11 by point A.

- Its mass can be reduced by approximately 20 % maintaining the same absorbed energy, by increasing the aluminium thickness up to 2.30 mm and reducing the GFRP thickness and the foam density to their lower bounds. This is graphically indicated in Figure 11 by point B.

Regarding the SEA–P_{peak} front, two characteristic regions could be observed in the studied range. Firstly, for optimum SEA between 10.5 kJ/kg and 16 kJ/kg, the optimum pairs are obtained using a foam density of 105 kg/m^3, a GFRP thickness between 1.0 and 1.2 mm, and gradually increasing the aluminium thickness from 1 to 2.3 mm. Secondly, for 16 kJ/kg $\leq$ SEA $\leq$ 24 kJ/kg, the optimum pairs show a drop in the foam density to a value of 90 kg/m^3 and a progressive increase of the aluminium thickness, while keeping the GFRP thickness at its minimum. It can be also observed that the initial peak force can be significantly reduced in the original design without harming the SEA by reducing the foam density to 105 kg/m^3 and the GFRP thickness to 1.0 mm, and slightly reducing the aluminium thickness too. This is graphically indicated by point A in Figures 12a and 12b. Also, the specific energy absorption can be increased by approximately 38 %, keeping the component mass of the original design, i.e., 1.737 kg. As indicated by point B in Figure 12b, this is achieved by using an aluminium thickness of 2.7 mm, a foam density of 90 kg/m^3 and a GFRP thickness of 1 mm.

4.2. Case II: Foam loaded in its strong direction

The goodness estimators used to check the accuracy of the surrogate models are provided in Table 8. These indicators are in line with those obtained for the optimization case I.

Table 8: Goodness estimators of the MARS surrogate model fitted to the sample points in optimization case II. RMSE: root-mean-squared error, MeanAE: mean absolute error.

| Objective function	R^2	RMSE	MeanAE
Absorbed energy	0.9975	0.575 kJ	0.398 kJ
Mass	0.9999	1.070×10^{-4} kg	5.160×10^{-5} kg
Specific energy absorption	0.9929	0.276 kJ/kg	0.207 kJ/kg
Initial peak load	0.997	3.547 kN	2.703 kN
Crush force efficiency	0.8691	0.195	0.116

For case II, Pareto fronts are presented in Figures 13 and 14. Similar conclusions to case I can be drawn from the optimum results regarding the E_a–m front: the performance of the part can be improved in one way or another by using the strong direction of the foam and reducing the foam density and the GFRP thickness to their lower bounds (points A and B in Figure 13). The point beyond which it is worth increasing the GFRP thickness appears later in Figure 13b than in Figure 11b, given that the foam is used more effectively now.

Some differences must be highlighted when it comes to the SEA–P_{peak} optimum sets, compared to what was presented in Figure 12. Here, optimum specific energy absorptions are achieved firstly by increasing the aluminium thickness and the foam density (for $15\,\text{kJ/kg} \leq SEA \leq 19\,\text{kJ/kg}$, approximately) up to an approximate value of $190\,\text{kg/m}^3$, if a simultaneous minimization of the peak load is pursued. For higher values of optimum specific energy absorption minimizing the peak load, the density of the foam should be kept at its lower bound –with an exception for $20\,\text{kJ/kg} \leq SEA \leq 22\,\text{kJ/kg}$– and the aluminium thickness should be progressively increased. It is worth mentioning that these latter designs where the foam drops to its minimum density and the extrusion increases its thickness have an initial peak load which could be too high for a car crash box.

The design proposed in [30] can be improved keeping one of the objectives constant. If the initial peak force is to be reduced, the same SEA can be maintained by just placing the foam in its strong direction and reducing its density to the minimum. The thicknesses of the aluminium and the GFRP must also be reduced to their minima in this case, which is indicated by the letter A in Figure 14. This enables a considerable reduction in the
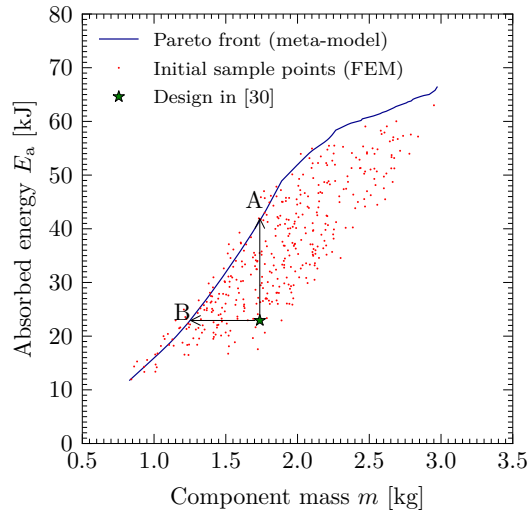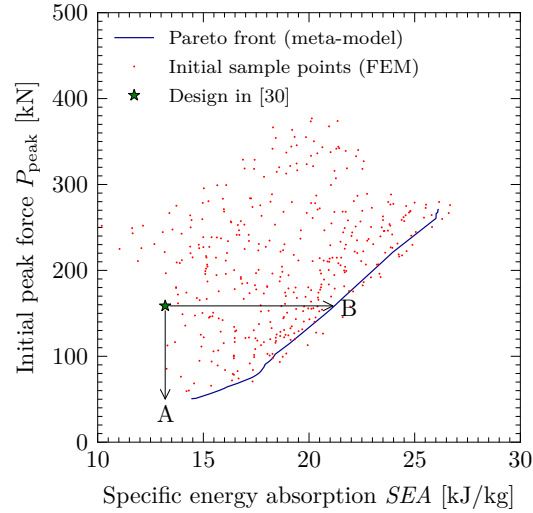
(a) Pareto front for optimization case II considering the absorbed energy and the mass of the component as objective functions.
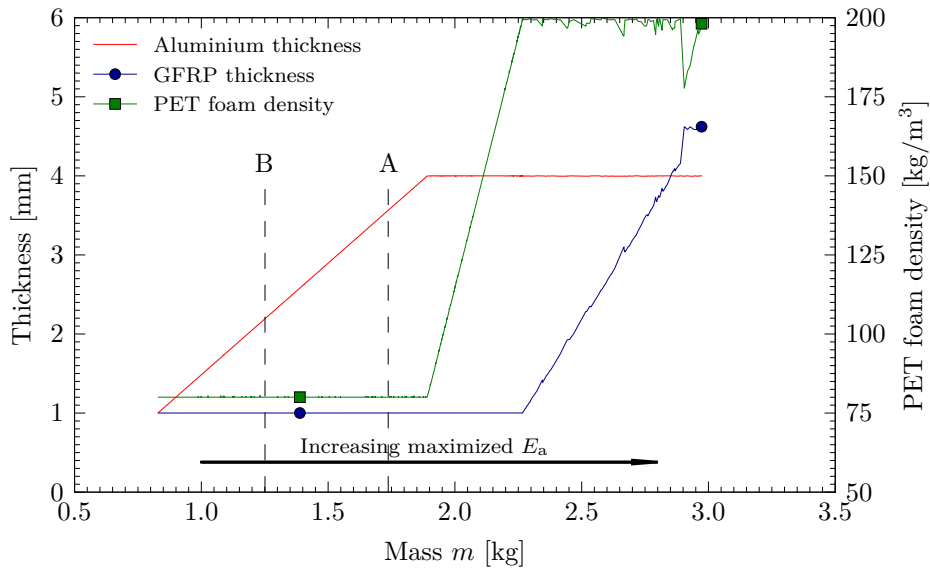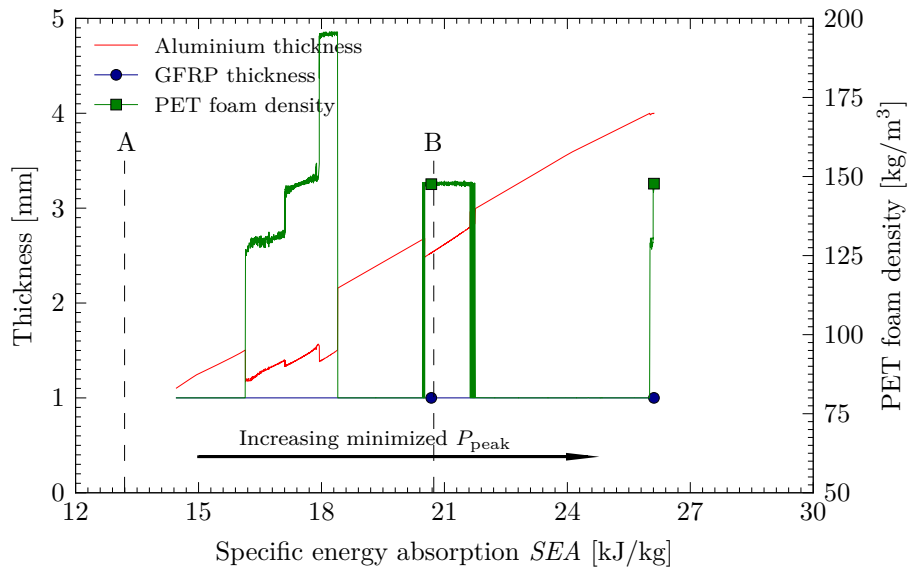

(b) Evolution of the three design variables along the Pareto front. Projection on the mass function.

Figure 13: Optimization results for case II considering the absorbed energy E_a and the component mass m as objective functions. Pareto set and evolution of the design variables.

(a) Pareto front for optimization case II considering the specific energy absorption and the initial peak load as objective functions.

(b) Evolution of the three design variables along the Pareto front. Projection on the specific energy absorption function.

Figure 14: Optimization results for case II considering the specific energy absorption and the initial peak load as objective functions. Pareto set and evolution of the design variables.

initial peak load to be achieved. Point A is out of range because it corresponds to the SEA of the experimental component, where the foam was placed in its weak direction. However, all the optimum designs for Case II were carried out with the foam in its strong direction. This explains why the point lies outside the Pareto front. On the other hand, if the specific energy absorption of the component is to be increased to its maximum while keeping the same initial peak force (point B in Figure 14), a foam must be used with a density of $150\,\text{kg/m}^3$ -placed in its strong direction-. In this case, the aluminium thickness should be $2.55\,\text{mm}$ and the GFRP thickness $1\,\text{mm}$.

## 5. Optimization using Hanssen's modified analytical formula

As described in Section 3.2, the modified Hanssen's equation can predict the mean crushing force of the studied components with a good degree of accuracy. This semi-empirical model was also used for the optimization of the absorbed energy and the mass of the component. The absorbed energy was obtained by multiplying the predicted mean crushing force by the total crushing length ($245\,\text{mm}$), and the mass was obtained from the dimensions of the parts and the material densities. The optimization was run for cases I and II, using the best-fitting parameters provided in Table 6 and the same evolutionary algorithm used for the MARS meta-model. The obtained optimum sets are given in Figure 15a (case I) and Figure 15b (case II), showing the similarity between the FE values and Hanssen's analytical prediction.

In view of Figure 15, Hanssen's modified equation was proved to be an accurate model for the optimization of the component. The analytical model appeared to be even more exact than the MARS model at some regions of the Pareto front for case II, where a small number of FE sample points lay outside the MARS front but were captured by the analytical prediction.

6. Conclusions

This work presented the numerical modelling and the multi-objective optimization of a crash box which was previously tested experimentally by the authors. The following conclusions can be drawn:

- The axial quasi-static crushing of the proposed component was successfully simulated by a numerical model calibrated with the material experimental data. Only a
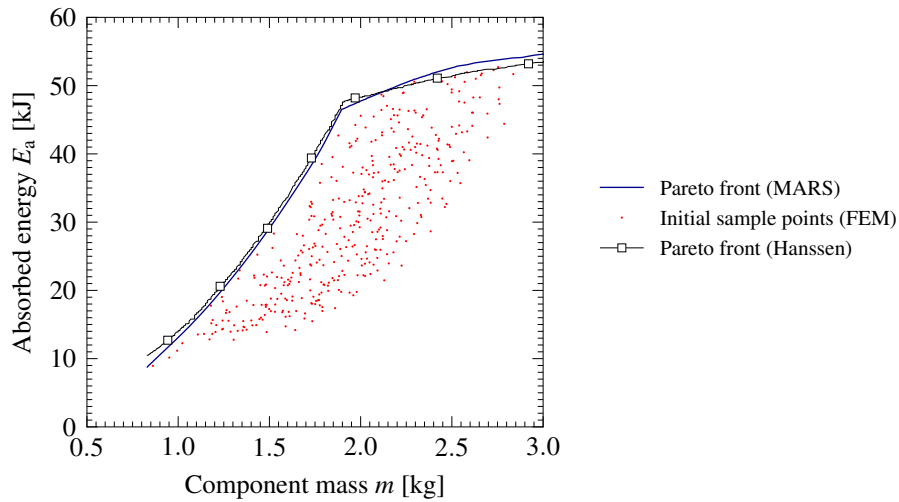
(a) Optimization of Hanssen's modified equation for case I. The Pareto front is compared with the one obtained with a MARS meta-model.
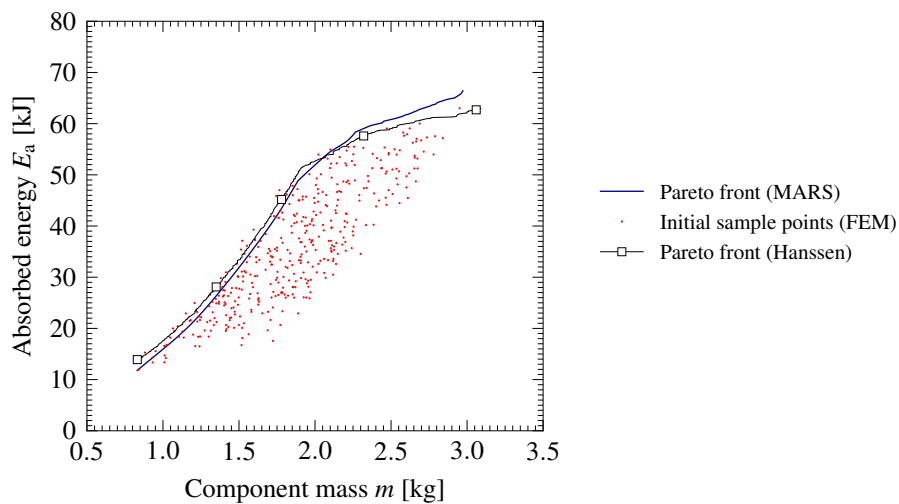
(b) Optimization of Hanssen's modified equation for case II. The Pareto front is compared with the one obtained with a MARS meta-model.

Figure 15: Comparison of the Pareto fronts obtained with Hanssen's modified analytical prediction and the MARS meta-model using the same evolutionary algorithm.

difference in the initial peak load was remarkable, which was caused by the misalignment of the GFRP plates in the experimental tests. The interaction effect appeared in the finite element model too, given that the response was very similar to the experimental behaviour.

- Surrogate models constructed with multivariate adaptive regression splines (MARS) accurately represented the response functions, with the single exception of the crush force efficiency. Therefore, these models could be safely used by the optimization algorithm.

- Two different multi-objective optimization cases were studied, where the foam was crushed along its strong or weak direction. It was shown that if the crushing of the foam was changed from the weak to the strong direction, the thickness of the aluminium tube could be reduced withouth decreasing the specific energy absorption.

- The modified Hanssen's analytical equation predicting the average crushing force of aluminium tubes filled with foam and GFRP inserts was fitted to the samples of the finite element model with a good degree of accuracy, in particular for foams with low yield strength. Optimum designs were obtained using this formulation and the evolutionary algorithm, and were compared to those predicted by the MARS meta-model. The semi-empirical model was able to provide optimum pairs of absorbed energy and the mass of the component with a similar degree of accuracy as the MARS model. The satisfactory results proved the ability of the modified analytical prediction to reproduce the average crushing force of a component with a combination of three materials.

- The thickness of the GFRP plates must be kept at a value of 1 mm, no matter which objective function is to be optimized. This indicates that a thickness of 1 mm is enough to enable the interaction with the foam and provide a good crashworthiness effect for the component, and that the GFRP plates are useful only to trigger this interaction effect.

7. Acknowledgements

[1] S. R. Reid and T. Y. Reddy. Axial crushing of foam-filled tapered sheet metal tubes. *International Journal of Mechanical Sciences*, 28(10):643–656, 1986.

[2] S. R. Reid, T. Y. Reddy, and M. D. Gray. Static and dynamic axial crushing of foam-filled sheet metal tubes. *International Journal of Mechanical Sciences*, 28(5): 295–322, 1986.

[3] W. Abramowicz and T. Wierzbicki. Axial crushing of foam-filled columns. *International Journal of Mechanical Sciences*, 30(3-4):263–271, 1988.

[4] M. Seitzberger, F.G. Rammerstorfer, H.P. Degischer, and R. Gradinger. Crushing of axially compressed steel tubes filled with aluminium foam. *Acta Mechanica*, 125 (1-4):93–105, 1997.

[5] M. Langseth, O.S. Hopperstad, and A.G. Hanssen. Crash behaviour of thin-walled aluminium members. *Thin-Walled Structures*, 32(1-3):127–150, 1998.

[6] A.G. Hanssen, M. Langseth, and O.S. Hopperstad. Static and dynamic crushing of square aluminium extrusions with aluminium foam filler. *International Journal of Impact Engineering*, 24(4):347 – 383, 2000.

[7] A.G. Hanssen, M. Langseth, and O.S. Hopperstad. Static and dynamic crushing of circular aluminium extrusions with aluminium foam filler. *International Journal of Impact Engineering*, 24(5):475 – 507, 2000.

[8] A.G. Hanssen, M. Langseth, and O.S. Hopperstad. Optimum design for energy absorption of square aluminum columns with aluminum foam filler. *International Journal of Mechanical Sciences*, 43(1):153–176, 2001.

[9] S. P. Santosa, T. Wierzbicki, A. G. Hanssen, and M Langseth. Experimental and numerical studies of foam-filled sections. *International Journal of Impact Engineering*, 24(5):509–534, 2000.

[10] L. Yan, N. Chouw, and K. Jayaraman. Lateral crushing of empty and polyurethane-foam filled natural flax fabric reinforced epoxy composite tubes. *Composites Part B: Engineering*, 63:15 – 26, 2014.

[11] H.R. Zarei and M. Kröger. Crashworthiness optimization of empty and filled aluminum crash boxes. *International Journal of Crashworthiness*, 12(3):255–264, 2007.

[12] S. Hou, Q. Li, S. Long, X. Yang, and W. Li. Crashworthiness design for foam filled thin-wall structures. *Materials and Design*, 30(6):2024–2032, 2009.

[13] J. Bi, H. Fang, Q. Wang, and X. Ren. Modeling and optimization of foam-filled thin-walled columns for crashworthiness designs. *Finite Elements in Analysis and Design*, 46(9):698–709, 2010.

[14] G. Sun, G. Li, S. Hou, S. Zhou, W. Li, and Q. Li. Crashworthiness design for functionally graded foam-filled thin-walled structures. *Materials Science and Engineering A*, 527(7-8):1911–1919, 2010.

[15] S. Hou, X. Han, G. Sun, S. Long, W. Li, X. Yang, and Q. Li. Multiobjective optimization for tapered circular tubes. *Thin-Walled Structures*, 49(7):855–863, 2011.

[16] Y. Zhang, G. Sun, G. Li, Z. Luo, and Q. Li. Optimization of foam-filled bitubal structures for crashworthiness criteria. *Materials and Design*, 38:99–109, 2012.

[17] X. Song, G. Sun, G. Li, W. Gao, and Q. Li. Crashworthiness optimization of foam-filled tapered thin-walled structure using multiple surrogate models. *Structural and Multidisciplinary Optimization*, 47(2):221–231, 2013.

[18] G. Zheng, S. Wu, G. Sun, G. Li, and Q. Li. Crushing analysis of foam-filled single and bitubal polygonal thin-walled tubes. *International Journal of Mechanical Sciences*, 87:226–240, 2014.

[19] J. Fang, G. Sun, N. Qiu, N.H. Kim, and Q. Li. On design optimization for structural crashworthiness and its state of the art. *Structural and Multidisciplinary Optimization*, 55(3):1091–1119, 2017.

[20] J. Bouchet, E. Jacquelin, and P. Hamelin. Static and dynamic behavior of combined composite aluminium tube for automotive applications. *Composites Science and Technology*, 60:1891–1900, 2000.

[21] E.H. Hanefi and T. Wierzbicki. Axial resistance and energy absorption of externally reinforced metal tubes. *Composites Part B: Engineering*, 27(5):387 – 394, 1996.

[22] J. M. Alexander. An approximate analysis of the collapse of thin cylindrical shells under axial loading. *Quarterly Journal of Mechanics and Applied Mathematics*, 13 (1):10–15, 1960.

[23] H.-W. Song, Z.-M. Wan, Z.-M. Xie, and X.-W. Du. Axial impact behavior and energy absorption efficiency of composite wrapped metal tubes. *International Journal of Impact Engineering*, 24(4):385–401, 2000.

[24] K.C. Shin, J.J. Lee, K.H. Kim, M.C. Song, and J.S. Huh. Axial crush and bending collapse of an aluminum/GFRP hybrid square tube and its energy absorption capability. *Composite Structures*, 57(1-4):279–287, 2002.

[25] M.R. Bambach and M. Elchalakani. Plastic mechanism analysis of steel SHS strengthened with CFRP under large axial deformation. *Thin-Walled Structures*, 45(2):159 – 170, 2007.

[26] M.R. Bambach, M. Elchalakani, and X.L. Zhao. Composite steel-CFRP SHS tubes under axial impact. *Composite Structures*, 87(3):282–292, 2009.

[27] M.R. Bambach, H.H. Jama, and M. Elchalakani. Static and dynamic axial crushing of spot-welded thin-walled composite steel–cfrp square tubes. *International Journal of Impact Engineering*, 36(9):1083 – 1094, 2009.

[28] M. Costas, J. Díaz, L.E. Romera, S. Hernández, and A. Tielas. Static and dynamic axial crushing analysis of car frontal impact hybrid absorbers. *International Journal of Impact Engineering*, 62:166–181, 2013.

[29] M. Costas, J. Díaz, L. Romera, and S. Hernández. A multi-objective surrogate-based optimization of the crashworthiness of a hybrid impact absorber. *International Journal of Mechanical Sciences*, 88:46–54, 2014.

[30] M. Costas, D. Morin, M. Langseth, L. Romera, and J. Díaz. Axial crushing of aluminum extrusions filled with PET foam and GFRP. An experimental investigation. *Thin-Walled Structures*, 99:45–57, 2016.

[31] E. Voce. The relationship between stress and strain for homogeneous deformations. *Journal of the Institute of Metals*, 74:537–562, 1948.

[32] W.L. Kolmogorov. Spannungen deformationen bruch. *Metallurgija*, page 230, 1970.

[33] H. Hooputra, H. Gese, H. Dell, and H. Werner. A comprehensive failure model for crashworthiness simulation of aluminium extrusions. *International Journal of Crashworthiness*, 9(5):449–464, 2004.

[34] *ABAQUS 6.13 Documentation*. Dassault Systèmes, Providence Road, Rhode Island, 2014.

[35] BASF. Ultramid (r) A3WG10 BK00564 Polyamide 66. Product information sheet, April 2015.

[36] V.S. Deshpande and N.A. Fleck. Isotropic constitutive models for metallic foams. *Journal of the Mechanics and Physics of Solids*, 48(6):1253–1283, 2000.

[37] ISO. Rigid cellular plastics – Determination of compression properties. ISO 844:2014, International Organization for Standardization, Geneva, Switzerland, 2014.

[38] J. Ma, D. Hou, Y. Chen, and Z. You. Quasi-static axial crushing of thin-walled tubes with a kite-shape rigid origami pattern: Numerical simulation. *Thin-Walled Structures*, 100:38 – 47, 2016.

[39] Armacell. Armaform PET/W AC, technical data, March 2014.

[40] M. Costas. *Crashworthiness analysis and design optimization of hybrid impact energy absorbers*. PhD thesis, GME - Group of Structural Mechanics, Universidade da Coruña, 2016.

[41] J. H. Friedman. Multivariate adaptive regression splines. *Annals of Statistics*, 19: 1–141, 1991.

[42] J.H. Friedman and C.B. Roosen. An introduction to multivariate adaptive regression splines. *Statistical methods in medical research*, 4(3):197–217, 1995.

[43] A. Forrester, A. Sobester, and A. Keane. *Engineering Design via Surrogate Modelling: A Practical Guide*. Wiley, Hoboken (New Jersey), USA, 2008.

[44] J. E. Eddy and K. Lewis. Effective generation of Pareto sets using genetic programming. *Proceedings of ASME Design Engineering Technical Conference*, 2001.